Supporting Information

Weber et al. 10.1073/pnas.1421322112

SI Materials and Methods

Details on Experimental Assay.

Experimental settings.

Protein preparation. G-actin solutions were prepared by dissolving lyophilized G-actin in deionized water and dialyzing against fresh G-buffer (2 mM Tris, 0.2 mM ATP, 0.2 mM $CaCl_2$, 0.2 mM DTT, and 0.005% NaN_3) overnight at 4 °C. Polymerization of actin was initiated by adding 10% of the sample volume of a 10-fold concentrated F-buffer (20 mM Tris, 20 mM $MgCl_2$, 2 mM DTT, and 1 M KCl). For fluorescence microscopy, fluorescently labeled filaments stabilized with Alexa Fluor 488 phalloidin (Invitrogen) were used. HMM is prepared from myosin II obtained from rabbit skeletal muscle following a standardized protocol.

Sample preparation. Flow chambers that consist of coverslips (Carl Roth) fixed to microscope slides (Carl Roth) by parafilm were prepared. The coverslips were coated with a 0.1% nitrocellulose solution, which was made by diluting a 2% (vol/vol) solution (Electron Microscopy Sciences) in amyl acetate (Roth), and were left to dry overnight before constructing the flow chambers. The chamber has a volume of ∼30 μL, and its size is typically three orders of magnitude larger than the length of a single filament to prevent boundary effects. Before an experiment, both actin and HMM were diluted in assay buffer (25 mM imidazolhydrochloride, pH 7.4, 25 mM KCl, 4 mM $MgCl_2$, 1 mM EGTA, and 1 mM DTT). The flow chamber is incubated with the HMM dilution, and the surfaces are passivated with a BSA solution [10 mg/mL BSA (Sigma) dissolved in assay buffer], before the insertion of the actin dilution. To initiate the experiment, 2 mM of ATP dissolved in assay buffer is inserted into the flow chamber along with a standard antioxidant buffer supplement GOC [2 mg glucose-oxidase (Sigma) and 0.5 mg Catalase (Fluka)] to prevent oxidation of the fluorophore. After adding all components, the flow chamber was sealed with vacuum grease (Bayer Silicones).

Image acquisition and preprocessing. All of the data are acquired on a Leica DMI 6000B inverted microscope with a 100× oil objective (numerical aperture: 1.4). Images (resolution: 1,344 × 1,024 pixels) were captured with a CCD camera (C4742-95; Hamamatsu) via a 1.0 camera mount. The image processing software OpenBox was used to acquire and store images. Image processing was carried out before the curvature analysis with ImageJ. A time overlay of the images was subtracted from each image to neglect nonmoving filaments. Then, background subtraction and conversion to binary image were performed.

Video analysis: obtaining coordinates. Filaments are identified by labeling connected components in the binary images and then are skeletonized using Matlab. A cubic spline fit is applied to the skeletonized filaments to obtain subpixel resolution of the filament contour coordinates (Movies S1–S3). The coordinates are used to determine the curvature of segments along the filament contour (*Materials and Methods*).

Impact of segment length and spline fit on curvature distribution.

Impact of segment length for active case. For a thermal filament, the curvature distribution strongly depends on the segment length Δs (35). In stark contrast, an active filament does not show any dependence, as can be seen in Fig. S1. Note that this statement only applies if Δs is much smaller than the filament length L; otherwise, any Δs dependence can be traced back to a too rough discretization of the spline contour.

Impact of spline fit. Unlike in the simulation, where every segment of the filament is regarded as a bead with a well-defined coordinate, the precise coordinates of the actin contour cannot be obtained in the experiments due to resolution of the images used. Note that even with an image with infinite resolution would not help in obtaining the precise coordinates for the experiment because the actin filament image is constituted by an intensity distribution instead of well-defined bead coordinates. For this reason, as mentioned in the previous section, the image of fluorescently labeled actin filaments are converted into binary images which are then skeletonized. This procedure refers to the removal of pixels on the boundaries of objects until the objects become a line without it breaking apart. To this end, we used Matlab with a standard library "bwmorph" (37). Here, the skeletonized coordinates give rise to false curvatures due to its pixel resolution; hence, a spline fit is necessary. The coordinates obtained from the skeletonized image are spline fitted to extract the contour coordinates in subpixel resolution.

Evidently, the contour coordinates depend on the manner in which the spline fit is applied, namely the number of interpolating points used for the spline fit (N_{sp}). Especially when dealing with active filaments where large curvatures can emerge, the impact of N_{sp} on the resulting contour coordinates is not negligible, and thus the curvature is sensitive to N_{sp}.

Here, the effect of N_{sp} on the curvature distribution for active actin filaments is investigated, as can be seen in Fig. S2. Also, the obtained contour coordinates are visually scrutinized by plotting them on the actual image of the actin filament (Fig. S2). This procedure was implemented to minimize the curvature noise generated by the spline fitting. For $N_{sp} = 1,2$ the images show zigzagged wriggles of the contour (reconstructed from the spline fit coordinates), which are obviously artificial. Most importantly, these wiggles have a strong impact on the curvature distribution. The same applies to $N_{sp} = 10,20$. In this case, too many points are being used that the filament; thereby, the contours are not appropriately reproduced, resulting effectively in a stiffer filament. As for $N_{sp} = 4$, wriggles still exist, and for $N_{sp} = 7$, large curvatures are gradually cut off; therefore, we used $N_{sp} = 5$ for all results present throughout this work.

The validity of the visually obtain value $N_{sp} = 5$ is further examined by investigating the effect of N_{sp} for the case of thermal actin filaments (Fig. S3). Only for N_{sp} around 5, rescaling the curvature by $\kappa \to \kappa\sqrt{\ell_p \Delta s}$ (ℓ_p, persistence length; Δs, segment length) leads to a collapse of the curvature distributions on a single curve (35). For N_{sp} below 5, the contours are zigzagged and therefore easily seen to be inadequate (Fig. S2, *Upper Left*). Also, increasing N_{sp} above 5 artificially stiffens the contour, and again large curvatures are being lost in the spline fit process. Therefore, for $N_{sp} = 7,10$, the collapse is absent because larger curvatures are being lost during the spline fit process. Finally, for $N_{sp} = 5$, we find a value of the persistence length of about 14.7 μm, which is consistent with the literature (31).

We would like to emphasize that we checked all choices for N_{sp} to minimize artifacts in the data analysis. In the case of active filaments, this was done by overlapping the spline fitting curve onto the contour for many filament. We believe there is no other way in which one can choose the optimal N_{sp}. Recall that even with infinite resolution, the true coordinates cannot be obtained in the experiments, unlike in the simulations. The spline fitting method therefore aims to minimize analysis artifacts to enable the capture of curvature values at the length scales comparable to the resolution (≈ 0.06 μm) to a tolerable degree. Thus, at lengths significantly smaller than 0.06 μm, this method may fail.

Tangent-tangent correlations. We also analyzed the tangent-tangent correlations along the filament contour for the active and the

thermal case (see Fig. S4). Active actin filaments driven by HMM show a stronger decay of tangent correlations compared with the thermal case. Moreover, the decrease seems to be inconsistent with an exponential decay, whereas the tangent-tangent correlations for the thermal case agree with an exponential decay on a characteristic length scale given by the thermal persistent length ℓ_p. The finding for the active case seems to be in qualitative agreement with the decay of the correlation function predicted in ref. 33.

Details on the Computational and Kinetic Model.

Stochastic computational model. The computational model treats the polymer as N discretized beads of size d, which are coupled by harmonic springs for tangential stretching and bending. For bending forces along the polymer contour, we use the well-established Worm-like Chain model (25, 36), with the bending force at bead i given by

$$\mathbf{F}_i^{\text{bend}} = \frac{\mathcal{E}}{d}\,\frac{\partial}{\partial \mathbf{x}_i}\sum_j \mathbf{T}_j \cdot \mathbf{T}_{j+1}, \qquad \text{[S1]}$$

where $\mathbf{T}_i(t)$ denotes the tangent of the ith bead, defined as $\mathbf{T}_i = \mathbf{x}_i - \mathbf{x}_{i-1}/|\mathbf{x}_i - \mathbf{x}_{i-1}|$, and $\mathcal{E}$ (energy × length) is the bending rigidity. Each bead is exposed to uncorrelated thermal fluctuations $\xi(t)$

$$\left\langle \xi_i(t)\xi_j(t')\right\rangle = 2\mu k_b T\delta(t-t')\delta_{ij}, \qquad \text{[S2]}$$

where μ denotes the hydrodynamic mobility of the bead. We neglect filament stretching by choosing the corresponding spring constant K_c much larger than $\mathcal{E}/d^2$; thereby, the only quantities characterizing the thermal filament dynamics are the persistence length $\ell_p = \mathcal{E}/k_bT$ and the longest relaxation time (31, 38)

$$\tau_0 = \frac{\zeta}{\ell_p k_B T}(L/4.73)^4, \qquad \text{[S3]}$$

where $L = Nd$ is the filament length, and ζ denotes the friction coefficient of the considered rod segment. Note that the factor 4.73 arises from analytic calculations (38). We chose the parameters according to experimental measurements for actin (31), with $\ell_p = 16$ μm and $\tau_0 \approx 0.5$ s for $L = 6$ μm.

We simplify the interactions between the filament and the 2D motor lawn to a process of stochastic and independent binding events of motors along the filament contour. (We find similar results when explicitly modeling the 2D motor lawn. However, the simplification to stochastic binding event along the filament contour essentially reduced the CPU time and thereby allows the acquisition of a sufficient amount of statistics. Moreover, this assumption helps to simplify the picture concerning what is necessary for the anomalous curvature buildup.) A motor begins its cycle with the cross-linking phase by binding randomly at bead i (with coordinates $\mathbf{x}_i$) with probability $1/N$, independent of the bead's binding history or state occupancy. After attaching to the filament, say at time $t = 0$, the motor attains the spatial coordinates of the randomly selected bead. The motor stays in this configuration, called the cross-linking phase, for a time period $\tau_\times$. During this time period the motor provides a rigid link between substrate and filament for displacements beyond the capture length l_c (Fig. 2 *A–C*). Specifically, the corresponding restoring force is zero for $|\mathbf{x}_i(0) - \mathbf{x}_i(t)| < l_c$, and proportional to $K_\times$ for $|\mathbf{x}_i(0) - \mathbf{x}_i(t)| \geq l_c$ [harmonic force $\mathbf{F}_i^\times$ pointing parallel to $\mathbf{x}_i(0) - \mathbf{x}_i(t)$, and with $K_\times \approx K_c$]. After the cross-linking phase, the subsequent pushing phase includes the power stroke of the molecular motor. It is modeled as a spring that is connected to the filament, which exerts a force $\mathbf{F}_i^s$ on the filament while moving with a velocity $\Delta x_s/\tau_s$ (Δx_s denotes the stroke length) within the stroke time τ_s along its contour. For simplicity, we use a linear spring with a constant $K_s \approx K_c$. A typical filament in the experiment is about 6 μm in length, and the stroke displacement has been estimated by measurements to be about 5 nm (28). Moreover, we matched the time scales characterizing the molecular motor, i.e., $\tau_\times = 0.001$ s and $\tau_s/\tau_\times = 0.1$ (28), with the thermal relaxation time $\tau_0 : \tau_0/\tau_\times \approx 5 \cdot 10^2$.

Finally, we checked that fluctuations of the number of bound motors in time do not have any qualitative impact on the ensuing filament dynamics; therefore, we kept the number of bound motors, denoted as m_b, constant. Apart from thermal fluctuations, the only (please note that motors do not act synchronously in our computational model; initial starting times of the binding cycle are randomized) stochastic element in our model is where (at which bead) the motor binds to the filament.

To check the results obtained by our simulation model for robustness against changes in the motor-filament interaction, we also simulated the filament dynamics in the extreme case where cross-links were absent. As shown in Fig. S5, this also results in an exponential tail.

By means of the model, we can address the role of the cross-linking (or holding) on the dynamics of the driven actin filament. To this end, we calculated the mean filament velocity v (Fig. S6*A*). In the absence of holding, i.e., motors just push, the mean velocity increases linear as a function of the number of bound motors m_b, with a slope given by $\Delta x_s/\tau_\times$ ($\tau_\times$, time of cross-linking phase; Δx_s, displacement of power-stroke). In the presence of holding, we observe a saturation with m_b, consistent with former experimental investigations (24, 39–45). We conclude that holding constitutes an essential determinant for the dynamics of the driven actin filaments. Regarding our model, the plateau value of v for large motor densities increases with the capture length l_c.

Additionally, we used the model to investigate the impact of holding on the short-time scaling coefficient α [$\delta R^2 \propto t^\alpha$ (main text); Fig. S6*B*]. In the absence of holding, $\alpha = 1$, independent of the number of bound motors m_b. In contrast, when motors push and cross link, α increases gradually with motor density m_b and capture length l_c. However, in the regime of reasonable parameters for the experimental system, e.g., $m_b \sim 5-20$ and $l_c \sim 20-40$ nm, the scaling coefficient α seems to be quite robust and close to 1. The existing deviation of α in the aforementioned parameter regime could not be distinguished experimentally.

Force and active motor size distribution. We also determined the cluster size of motors performing a power stroke along the filament contour. The cluster size s_{cl} of active motors is defined as the number of motors performing a power stroke that are in the direct neighborhood along the filament. The result for the corresponding probability distribution $\mathcal{P}(s_{cl})$ is shown in Fig. S7. We find that the distribution of active motors decays exponentially. This exponential decay is a direct result of the model definition, where motors are assumed to attach randomly and independently along the filament contour, which immediately implies an exponential distribution of sizes of bound motor clusters along the filament. Moreover, because the stroke phase is a subphase of the bound state, the distribution of active motors decays exponentially as well.

We cannot exclude that the exponential distribution of active motor clusters (Fig. S7) is related to the exponential curvature distribution (Fig. 1*C*). To make this connection, one needs to develop a microscopic theory for the mechanical forces generated by the active motor clusters and how those affect (on a coarse-grained level) the filament's curvature distribution. It would need to account for the subtle interplay between local forces generated by molecular motors and stress propagation along the filament. We could envision that such a theory would need to generalize earlier works on stress propagation along semiflexible polymers (32, 46–50).

Furthermore, we computed the distribution of forces longitudinal to the filament contour. We find that the longitudinal forces are distributed according to a Gaussian (Fig. S8).

Kinetic description.

Analytic solution. The kinetic equation for the curvature PDF

$$0 = D_\kappa \partial_\kappa^2 P(\kappa) + \frac{\lambda}{\eta} P(\kappa/\eta) - \lambda P(\kappa), \qquad \textbf{[S4]}$$

has an analytic solution in Fourier space (21, 22, 51)

$$\hat{P}(k) = \int_{-\infty}^{\infty} \mathrm{d}\kappa \; \mathrm{e}^{ik\kappa} P(\kappa) = \prod_{m=0}^{\infty} \left[1 + k^2 \eta^{2m}\right]^{-1}, \qquad \textbf{[S5]}$$

where we rescaled Eq. **S4** by $\kappa \to \kappa/\sqrt{D_\kappa \lambda^{-1}}$. After choosing the coefficients as mentioned in the main text, back-transformation leads to the red solid line depicted in Fig. 1*C*.

The limits $\eta \to 0$ and $\eta \to 1$. The following explanations for the limits has been essentially shown in refs. 20–22. Here, we concisely summarize the arguments allowing understanding of which distribution emerges in each of the two limiting cases, i.e., $\eta \to 0$ and $\eta \to 1$.

The moments $M_n = \int \mathrm{d}\kappa \kappa^n P(\kappa)$ can be computed from the recursion relation

$$M_n = n(n-1)(1-\eta^n)^{-1} M_{n-2}, \qquad \textbf{[S6]}$$

leading to $M_{2n} = (2n)! \prod_{k=1}^{n} [1-\eta^{2k}]^{-1}$. From this equation, the limit $\eta \to 0$ can be easily performed, leading to all even moments $M_{2n} = (2n)!$, which are equal to those of an exponential function in $\kappa \in [0, \infty)$. In particular, the kurtosis yields $\kappa_4 := \langle \kappa^4 \rangle / \langle \kappa^2 \rangle^2 = 6$.

In the limit $\eta \to 1$, the procedure is a bit more intricate. The even moments, given by $M_{2n} = (2n-1)!!(1-\eta)^{-n}$, diverge in this case. Note that the double factorial is defined as $(2n-1)!! = \prod_{m=1}^{n}(2m-1)$. Even though not directly obvious from Eq. **S4**, the singularity encountered in the moments explains why setting $\eta = 1$ in Eq. **S4** is not well defined. However, the limit $\eta \to 1$ can be accomplished by expanding the term $(1/1-\epsilon)P[\kappa/(1-\epsilon)]$ into a Taylor series around $\epsilon = 1-\eta = 0$, yielding $P(\kappa) + [P(\kappa) + \kappa P'(\kappa)]\epsilon + \mathcal{O}(\epsilon^3)$. Plugging this series into Eq. **S4** leads to a Gaussian distribution as a solution, $P(\kappa) \propto \exp(-\epsilon\kappa^2/2)$, with κ denoting the rescaled curvature $\kappa \to \kappa/\sqrt{D_\kappa \lambda^{-1}}$.

The Gaussian limit for $\eta \to 1$ also becomes obvious when considering the kurtosis as a function of η, which is given by $\kappa_4 = 6/(1+\eta^2)$. For $\eta \to 1$, $\kappa_4 = 3$, which is exactly the value expected for a Gaussian distribution. Taken together, $\eta \to 0$ lead to an exponential curvature distribution, whereas the limit $\eta \to 1$ corresponds to a Gaussian.

It is worth noting that the coefficient η in the kinetic model also determines the amount of energy dissipated relative to the energy input set by the curvature diffusion constant D_κ. Because the elastic energy of the filament scales as $\propto \kappa^2$ and $\kappa \to \eta\kappa$, the elastic energy as a function of η also scales as $\propto \eta^2$. Therefore, $1-\eta^2$ is the ratio of energy that is dissipated.

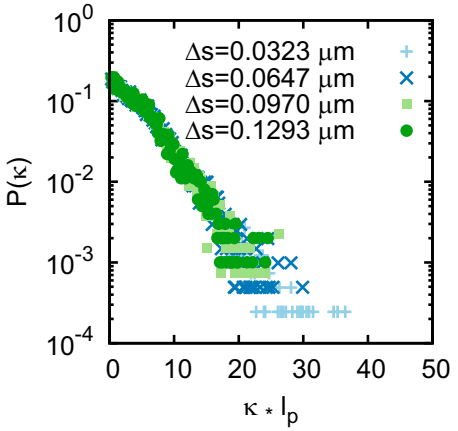

Fig. S1. Curvature distribution $P(\kappa)$ for different segment length Δs for the active actin filaments of length L in the range $4-10$ μm. For the segment length values Δs investigated, there is no dependence of the distribution on Δs. Parameters: $c = 1.5 \cdot 10^3$ μm^{-2}, $N_{sp} = 5$.

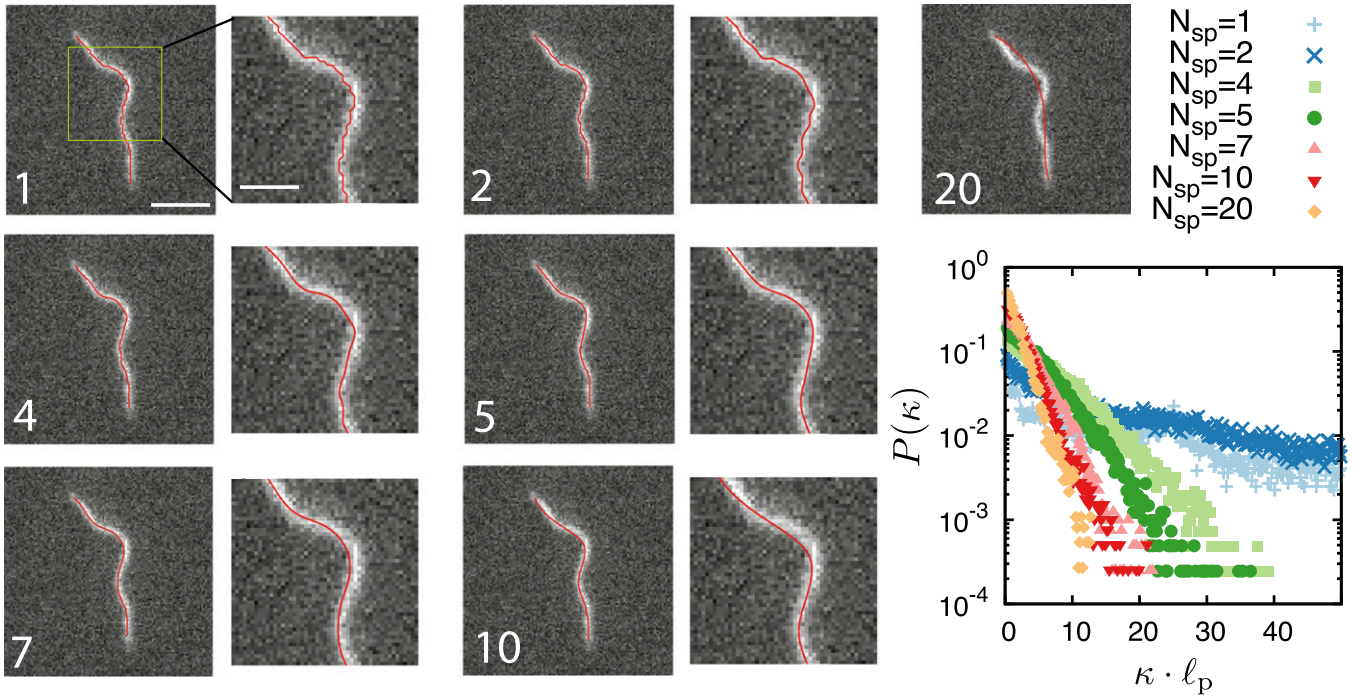

Fig. S2. Impact of the number of interpolating points N_{sp} on the curvature distribution (*Lower Right*); for each value of N_{sp}, a representative snapshot of the spline fit is depicted with the value indicated on the *Lower Left* of each snapshot. For $N_{sp} < 5$, zigzagged contours appear due to the lack of interpolating points. These zigzagged contours are inappropriate for the curvature analysis of active filaments. Increasing N_{sp} above 5 gradually cuts off the large curvatures that are crucial in the active filament case. This gradual elimination of large curvatures can also be seen in the curvature distribution. [Scale bars, 2 μm (1 μm for zoomed-in image).] Parameters: $c = 1.5 \cdot 10^3 \mu m^{-2}$.

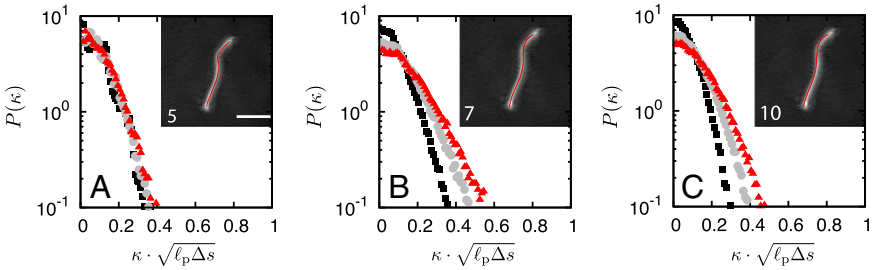

Fig. S3. Dependence of segment length Δs on the curvature distribution of thermal actin filaments for interpolation points for the spline fit (*A*) $N_{sp} = 5$, (*B*) $N_{sp} = 7$, and (*C*) $N_{sp} = 10$. For thermally fluctuating filaments, rescaling the curvature as $\kappa \to \kappa \cdot \sqrt{\ell_p \Delta s}$ resulted in the curvature distributions to collapse on a single curve (35), as shown in *A*. The collapse is not obtained for larger values of N_{sp}; see *B* and *C*. The *Inset* in each graph shows the contour obtained from the spline fit, with the N_{sp} value indicated at the *Lower Left* of each snapshot. For $N_{sp} = 7,10$, large local curvatures are being ignored because too many interpolating points are being used. Using too many interpolating points causes the rescaling to fail. (Scale bar, 5 μm.) Filament length $L = 10.9$ μm. Black squares, $\Delta s = 0.0835$ μm; gray circles, $\Delta s = 0.1670$ μm; red triangles, $\Delta s = 0.2505$ μm.

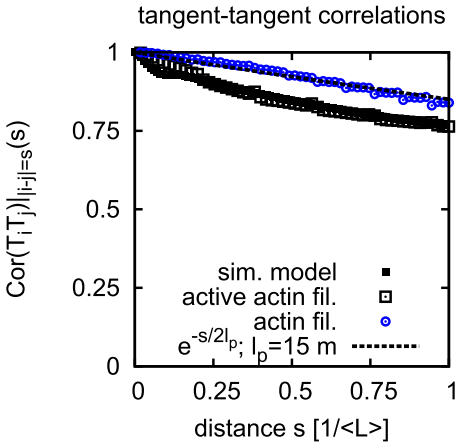

Fig. S4. Tangent-tangent correlations along the filament contour, parametrized by the contour *s*, are shown for active actin filaments moving in the motility assay (black) and a passive (thermal) actin filament (blue).

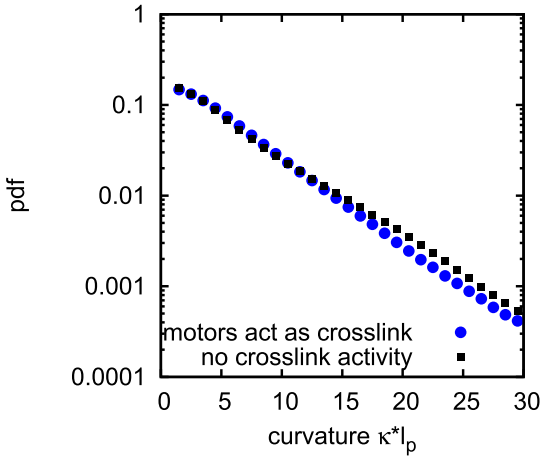

Fig. S5. Curvature PDF of the simulation model with motors acting as cross-links (blue dots) and in the absence of cross-linking activity (black squares). In both cases, the curvature distribution decays exponentially with only minor quantitative differences. Parameters: $m_b = 20$.

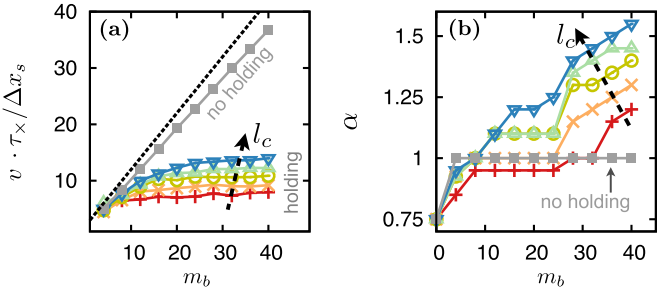

Fig. S6. (*A*) Results from the computational model for the mean filament velocity *v* (rescaled by $\Delta x_s/\tau_\times$; $\tau_\times$ time of cross-linking phase, displacement of power-stroke $\Delta x_s = 5$ nm) (28) against bound motors m_b. Only in the presence of cross-linking forces, a saturation is observed, with larger plateau values for larger l_c (from bottom to top: $l_c = \{4,6,8,10,12\} \cdot \Delta x_s$). Otherwise, $v \approx (\Delta x_s/\tau_\times) m_b$ (black dashed line). (*B*) Scaling coefficient α as a function of motor density m_b and for various values of the capture length l_c (obtained by computational model). Whereas α is independent of m_b in the absence of cross-linking (for the m_b values investigated), α increases gradually with motor density m_b and capture length l_c when modeling the motor with pushing and the cross-linking phase. However, for a reasonable choice of parameters for the gliding assay, e.g., $m_b \sim 5-20$ and $l_c \sim 20-40$ nm, the scaling coefficient α is close to 1. Please note that these weak deviations to $\alpha = 1$ in the aforementioned parameter regime could not be distinguished experimentally.

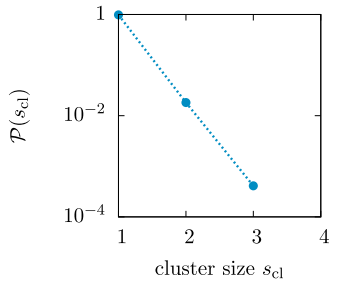

Fig. S7. Probability distribution $\mathcal{P}(s_{cl})$ of motors performing a power stroke that are in the direct neighborhood along the filament. $\mathcal{P}(s_{cl})$ decays exponentially. Parameters: $m_b = 22$.

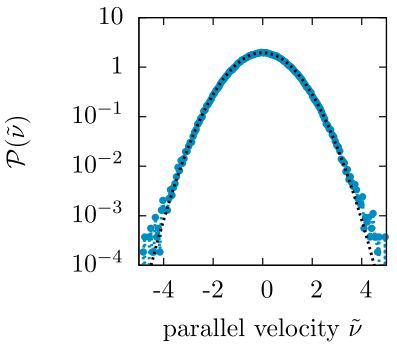

Fig. S8. Probability distribution $\mathcal{P}(\tilde{\nu})$ of the velocity parallel to the filament contour, $\tilde{\nu} = \nu/\sqrt{\mathrm{Var}(\nu)}$, where $\mathrm{Var}(\nu)$ denotes the variance. Forces longitudinal to the filament contour, which are proportional to the longitudinal velocity $\tilde{\nu}$ in our stochastic computer simulation, are distributed according to a Gaussian (see dotted line). Note that average velocity is not zero because the filament moves. Parameters: $m_b = 22$.

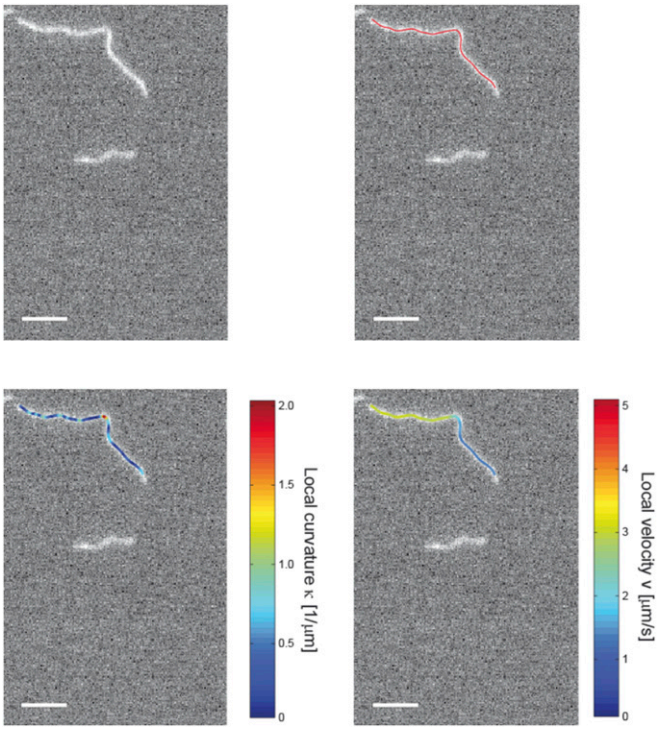

Movie S1. This movie depicts a representative filament dynamics, with *Upper Left* corresponding to the microscope images, *Upper Right* showing an additional spline fit to filament contour, *Lower Left* depicting the local curvature κ ($1/\mu m^2$) in color, and *Lower Right* showing the local velocity v (μ/s). Parameters: $c = 1.5 \cdot 10^3$ μm^{-2}, $L = 8.6$ μm. (Scale bars, 2 μm.)

Movie S1

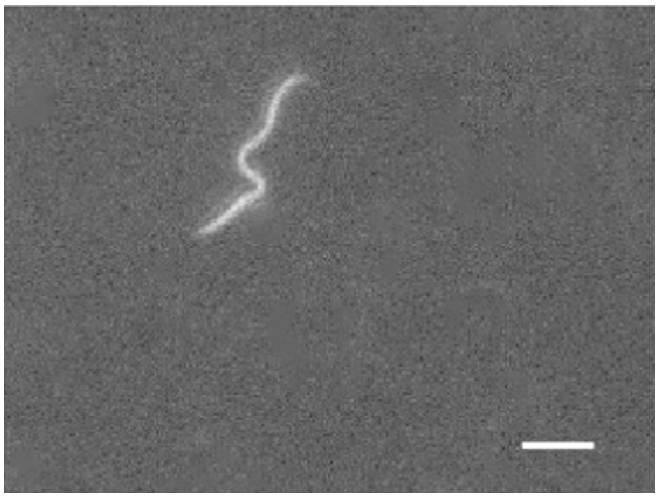

Movie S2. Several examples of large and anomalous curvature events found in the experiments. Parameters: $c = 1.5 \cdot 10^3$ μm^{-2}, $L = 4 - 11$ μm. (Scale bars, 2 μm.)

Movie S2

Movie S3. Representative dynamics of the filament given by the stochastic model. In the beginning, the filament performs solely Brownian fluctuation with $L = \ell_p/3$. Then, the motor-filament interaction is switched on, leading to the emergence of anomalous curvature events, as observed in the gliding assay experiments. Parameters: $L = \ell_p/3$, $l_c = 40$ nm, $m_b = 20$.

Movie S3